

Article

Two Faces of Water in the Formation and Stabilization of Multicomponent Crystals of Zwitterionic Drug-Like Compounds

Artem O. Surov ¹, Nikita A. Vasilev ¹, Andrei V. Churakov ² , Olga D. Parashchuk ³, Sergei V. Artobolevskii ⁴, Oleg A. Alatorsev ⁴, Denis E. Makhrov ⁴ and Mikhail V. Vener ^{2,4,*} 

¹ G.A. Krestov Institute of Solution Chemistry of RAS, 153045 Ivanovo, Russia; aos@isc-ras.ru (A.O.S.); nav@isc-ras.ru (N.A.V.)

² N.S. Kurnakov Institute of General and Inorganic Chemistry of RAS, 119991 Moscow, Russia; churakov@igic.ras.ru

³ Faculty of Physics, Lomonosov Moscow State University, 119991 Moscow, Russia; olga_par@physics.msu.ru

⁴ Department of Quantum Chemistry, D. Mendeleev University of Chemical Technology, 125047 Moscow, Russia; Artobolevskiy_Sergey_Vladimirovich@muctr.ru (S.V.A.); Olegalatorcev@muctr.ru (O.A.A.); Denis_Makhrov@muctr.ru (D.E.M.)

* Correspondence: venermv@muctr.ru



Citation: Surov, A.O.; Vasilev, N.A.; Churakov, A.V.; Parashchuk, O.D.; Artobolevskii, S.V.; Alatorsev, O.A.; Makhrov, D.E.; Vener, M.V. Two Faces of Water in the Formation and Stabilization of Multicomponent Crystals of Zwitterionic Drug-Like Compounds. *Symmetry* **2021**, *13*, 425. <https://doi.org/10.3390/sym13030425>

Academic Editor: Marek Szafranski

Received: 14 February 2021

Accepted: 3 March 2021

Published: 6 March 2021

Publisher's Note: MDPI stays neutral with regard to jurisdictional claims in published maps and institutional affiliations.



Copyright: © 2021 by the authors. Licensee MDPI, Basel, Switzerland. This article is an open access article distributed under the terms and conditions of the Creative Commons Attribution (CC BY) license (<https://creativecommons.org/licenses/by/4.0/>).

Abstract: Two new hydrated multicomponent crystals of zwitterionic 2-aminonicotinic acid with maleic and fumaric acids have been obtained and thoroughly characterized by a variety of experimental (X-ray analysis and terahertz Raman spectroscopy) and theoretical periodic density functional theory calculations, followed by Bader analysis of the crystalline electron density) techniques. It has been found that the Raman-active band in the region of 300 cm^{-1} is due to the vibrations of the intramolecular O-H...O bond in the maleate anion. The energy/enthalpy of the intermolecular hydrogen bonds was estimated by several empirical approaches. An analysis of the interaction networks reflects the structure-directing role of the water molecule in the examined multicomponent crystals. A general scheme has been proposed to explain the proton transfer between the components during the formation of multicomponent crystals in water. Water molecules were found to play the key role in this process, forming a “water wire” between the COOH group of the dicarboxylic acid and the COO⁻ group of the zwitterion and the rendering crystal lattice of the considered multicomponent crystals.

Keywords: 2-aminonicotinic acid; maleic and fumaric acids; intra- and inter-molecular hydrogen bonds; structure-directing role of water; periodic (solid-state) DFT computations; low-frequency Raman spectrum; water wires

1. Introduction

Most pharmaceutical compounds and materials for technological applications are designed and produced as organic molecular crystals [1,2]. The fundamental physicochemical properties and efficiency of these materials mainly depend on the nature of intermolecular interactions that are responsible for overall packing arrangements of the molecules or ions in periodic structures. Thus, the ability to control and modify the crystalline environment of a material without affecting its intrinsic chemical properties is of great importance to the development of new solid pharmaceutical forms and molecular devices [3,4]. Changing the packing arrangement of molecules in the solid state by introducing an additional component via the formation of a multicomponent crystal is a powerful strategy for improving and fine-tuning the most critical properties of a material, including its aqueous solubility and dissolution rate, physical stability, bioavailability, permeability, mechanical strength, melting point, etc. [5–10]. The main strategy of deliberate design of multicomponent crystals relies on the concept of supramolecular synthons [11,12], which are defined as spatial arrangements of intermolecular interactions [13] that occur in a repeatable and

predictable fashion, regardless of the availability of other functional groups [14]. The identification and understanding of appropriate intermolecular interactions that govern and control the molecular assembly through supramolecular synthons are the basis of crystal engineering [15,16]. The major drawback of the synthon approach to the crystal structure description, however, is that it does not account for the strength and/or importance of various interactions in controlling the resulting crystal structure. Since the packing patterns in single- and multi-component crystals are the result of the fine balance between all the noncovalent interactions in the material, a systematic quantitative assessment of the strength and nature of intermolecular forces responsible for the formation of supramolecular synthons is crucial as it provides a deeper insight into the fundamental principles that drive the formation of multicomponent molecular crystals and determine their properties.

A lot of attention has been recently paid to multicomponent crystals containing zwitterions and/or ions of drug-like compounds [17–22]. In such crystals, an 8-membered cycle with two short (strong) N+–H . . . O– bonds can be realized (Figure 2 in Reference [19]). This synthon, denoted as $R_2^2(8)$, has practically never been studied before [23–25], despite the fact that its energy is quite high (>50 kJ/mol [20]). The mechanism of formation of this synthon seems obvious, namely, it is formed through a proton transfer between an acid and a base along the N...H...O bond [19]. If one of the components is a zwitterion, the mechanism of proton transfer is more complicated and can involve solvent molecules (water or alcohol), which are often included in the resulting multicomponent crystals [18,20]. The transfer of an excess proton along the water wires has been studied in detail in many theoretical works [26–28], due to its realization in bio-systems [29–31]. As far as we know, there have been no theoretical works describing the proton transfer from dicarboxylic acid to a zwitterion of a drug-like compound in a polar protic solvent.

This work has three aims:

- (i). To characterize the structure and hydrogen bond (H-bond) network in two multicomponent crystals—[2AmNic+Mle+H₂O] (1:1:1) and [2AmNic+Fum+H₂O] (1:1:1)—by X-ray analysis, terahertz Raman spectroscopy, and periodic density functional theory (DFT) calculations. 2AmNic denotes 2-amino-nicotinic acid, while Mle and Fum stand for maleic and fumaric acids, respectively.
- (ii). To reveal the structure-directing role of the water molecule in the considered crystals.
- (iii). To theoretically substantiate the scheme of proton transfer from the dicarboxylic acid to the zwitterion by means of water wires.

2. Materials and Methods

2.1. Compounds and Solvents

The 2-aminonicotinic acid (C₆H₆N₂O₂, 98%) was purchased from Sigma-Aldrich, and the maleic (C₄H₄O₄, 98%) and fumaric acids (C₄H₄O₄, 98%) were bought from Merck. The solvents were purchased from various suppliers and were used as received without further purification.

2.2. Preparation Procedures

The grinding experiments were performed using a Fritsch planetary micro-mill, model Pulverisette 7, in 12 mL agate grinding jars with ten 5 mm agate balls at a rate of 500 rpm for 50 min. In a typical experiment, 100–120 mg of an equimolar 2-aminonicotinic acid/salt former mixture were placed into a grinding jar, and 40–50 μ L of water or a water/methanol mixture (1:1 *v:v*) were added with a micropipette. In another method, 200 mg of a 1:1 mixture of 2-aminonicotinic acid and a salt former were suspended in 3 mL of water and were left to be stirred on a magnetic stirrer at room temperature overnight. The precipitate was filtered from the solution and dried at room temperature. The identification of the solid forms obtained by different methods and estimation the solvent content were carried out by the X-ray powder diffraction (Supplementary Figures S1 and S2) and thermal analysis (Supplementary Figures S3 and S4).

The diffraction quality single crystals of fumarate and maleate salts of 2-aminonicotinic acid were obtained by dissolving 100 mg of a stoichiometric 1:1 mixture of the components in 12 mL of H₂O at 60 °C. After complete dissolution, the solution was gently cooled to the room temperature, covered by Parafilm with a few small holes pierced in it, and left for the solvent to evaporate. Small colorless crystals appeared in the solution after 5–7 days.

2.3. Thermal Analysis

2.3.1. Differential Scanning Calorimetry (DSC)

The thermal analysis was carried out using a differential scanning calorimeter with a refrigerated cooling system (Perkin Elmer DSC 4000, Waltham, MA, USA). The sample was heated in a sealed aluminum sample holder at a rate of 10 °C·min⁻¹ in a nitrogen atmosphere. The unit was calibrated with indium and zinc standards. The accuracy of the weighing procedure was ±0.01 mg.

2.3.2. Thermogravimetric Analysis (TGA)

The TGA was performed on a TG 209 F1 Iris thermomicrobalance (Netzsch, Selb, Germany). Approximately 10 mg of the sample was added to a platinum crucible. The samples were heated at a constant heating rate of 10 °C·min⁻¹ and purged throughout the experiment with a dry argon stream at 30 mL·min⁻¹.

2.4. Single Crystal and Powder X-ray Diffraction (XRD) Experiments

The single-crystal XRD data were collected on a SMART APEX II diffractometer (Bruker AXS, Karlsruhe, Germany) using graphite-monochromated MoK α radiation ($\lambda = 0.71073$ Å). Absorption corrections based on measurements of equivalent reflections were applied [32]. The structures were solved by direct methods and refined by full-matrix least-squares on F2 with anisotropic thermal parameters for all the non-hydrogen atoms [33]. All the hydrogen atoms were found from a difference Fourier map and refined isotropically. The crystallographic data for [2AmNic+Mle+H₂O] (1:1:1) and [2AmNic+Fum+H₂O] (1:1:1) were deposited by the Cambridge Crystallographic Data Centre as supplementary publications numbered 2,053,450 and 2,053,451. This information can be obtained free of charge from the Cambridge Crystallographic Data Centre at www.ccdc.cam.ac.uk/data_request/cif.

The X-ray powder diffraction (XRPD) data of the bulk materials were recorded under ambient conditions in Bragg-Brentano geometry with a Bruker D2 Phaser diffractometer equipped with a second-generation LynxEye detector with CuK α radiation ($\lambda = 1.5406$ Å).

2.5. Raman Spectroscopy

For the Raman measurements, all the powders were compressed into tablets. The Raman measurements in the spectral range of 10–440 cm⁻¹ were performed using a Raman microscope with the excitation wavelength 633 nm, provided by a He–Ne laser with the maximum power of 17 mW (inVia and RL633, Renishaw plc, Spectroscopy Product Division, Old Town Wotton-Under-Edge, Gloucestershire, UK). The 50 \times objective lens (Leica DM 2500 M, NA = 0.75, Leica Mikrosysteme Vertrieb GmbH Mikroskopie und Histologie Ernst-Leitz-Strasse 17-37, Wetzlar, Germany) was used. The measurements were made with a built-in double monochromator with dispersion subtraction in the confocal regime (NExT monochromator, Renishaw plc, Spectroscopy Product Division, Old Town Wotton-Under-Edge, Gloucestershire, UK). The acquisition time and number of accumulations for the Raman spectra were adjusted to maximize the signal-to-noise ratio with the minimal sample degradation. All the spectra for the powder samples were measured at several points and then averaged to reduce the anisotropy effect on the Raman spectra. The background from the Raman spectra was subtracted by the cubic spline interpolation method. All the spectra were divided by the number of accumulations and acquisition time. The dips in the spectra at wavenumbers of 23 cm⁻¹ and 304 cm⁻¹ are the artefacts of the measurements associated with the presence of dust particles on the NExT monochromator mirrors.

2.6. Periodic (Solid-State) DFT Computations

In the CRYSTAL17 calculations [34], the B3LYP (Becke 3-parameter, Lee-Yang-Parr) [35,36] and PBE (Perdew-Burke-Ernzerhof) [37] functionals were employed with 6-31G** all-electron Gaussian-type localized orbital basis sets. The London dispersion interactions were taken into account by introducing the D3 correction with Becke-Jones damping (PBE-D3) developed by Grimme et al. [38,39]. The structural relaxations were limited to the positional parameters of the atoms. In all cases, the experimental crystal structure with normalized X-H bond lengths was used as the starting point for geometry optimization. Further details of the calculations are given in Section S1 of Supplementary Materials.

The metric parameters of the H-bonded fragments in the considered crystals are better reproduced by B3LYP than PBE-D3 (Tables 1 and 2). The enthalpies/energies of intermolecular H-bonds calculated using the B3LYP and PBE-D3 approximations are compared in Supplementary Table S1. In accord with the literature [25], PBE-D3 overestimates the H-bonded energy. Thus, the B3LYP/6-31G** approximation was used to calculate the Raman spectra and estimate the H-bond energies in this work.

Table 1. Distances (Å) between the heavy atoms involved in the formation of intermolecular H-bonds and the angle (degree) of the O...H-X fragment, X = O or N, in [2AmNic+Fum+H₂O] (1:1:1). The experiment vs. the theoretical value. The periodic DFT computations were performed at different levels of approximation with fixed unit parameters.

Fragment ¹	Experiment	PBE-D3/6-31G**	B3LYP/6-31G**
O12 ... H21-N2	2.877 (175.7)	2.848 (176.4)	2.867 (176.0)
O11 ... H11-N1	2.662 (175.3)	2.668 (173.5)	2.681 (173.7)
O12 ... H31-O3	2.702 (174.4)	2.684 (177.9)	2.697 (178.0)
O13 ... H32-O3	2.859 (167.8)	2.801 (172.2)	2.828 (171.2)
O11 ... H14-O14	2.559 (164.0)	2.540 (160.6)	2.547 (161.9)
O3 ... H1-O1	2.582 (165.9)	2.545 (165.4)	2.571 (165.9)

¹ See Figure 1, the atomic numbering is borrowed from the cif file.

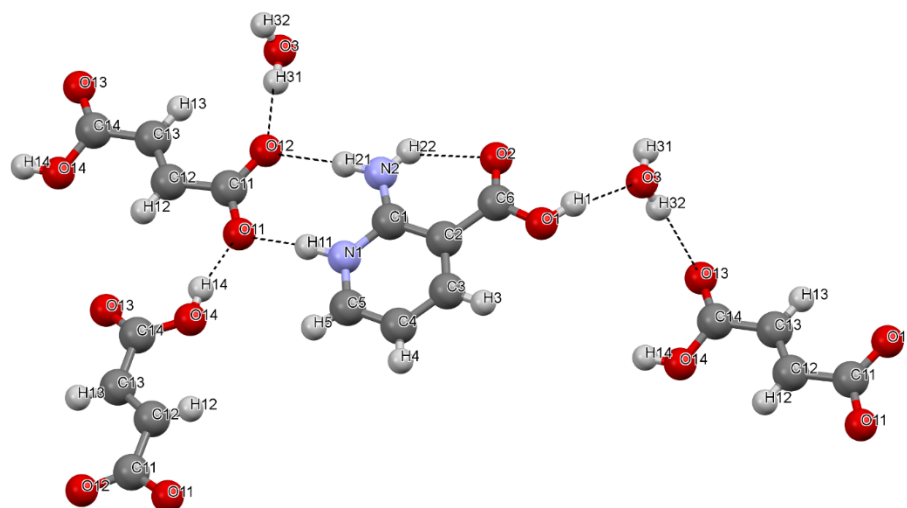


Figure 1. A fragment of the [2AmNic+Fum+H₂O] (1:1:1) crystal structure, illustration of hydrogen bond patterns.

Table 2. Distances (Å) between the heavy atoms involved in the formation of inter- and intra-molecular H-bonds and the angle (degree) of the O . . . H-X fragment, X = O or N, in [2AmNic+Mle+H₂O] (1:1:1). The experiment vs. the theoretical values.

Fragment ¹	Experiment	PBE-D3/6-31G**	B3LYP/6-31G**
O12 . . . H21-N2	2.816 (176.4)	2.804 (170.4)	2.811 (171.7)
O11 . . . H11-N1	2.816 (170.1)	2.816 (173.7)	2.818 (172.8)
O12 . . . H31-O3	2.717 (177.2)	2.701 (176.0)	2.706 (176.4)
O13 . . . H32-O3	2.771 (177.5)	2.701 (173.4)	2.706 (177.6)
O3 . . . H1-O1	2.567 (173.0)	2.536 (173.6)	2.550 (174.4)
O11 . . . H14-O14 (intra)	2.460 (174.9)	2.462 (176.1)	2.460 (174.9)

¹ See Figure 2, the atomic numbering is borrowed from the cif file.

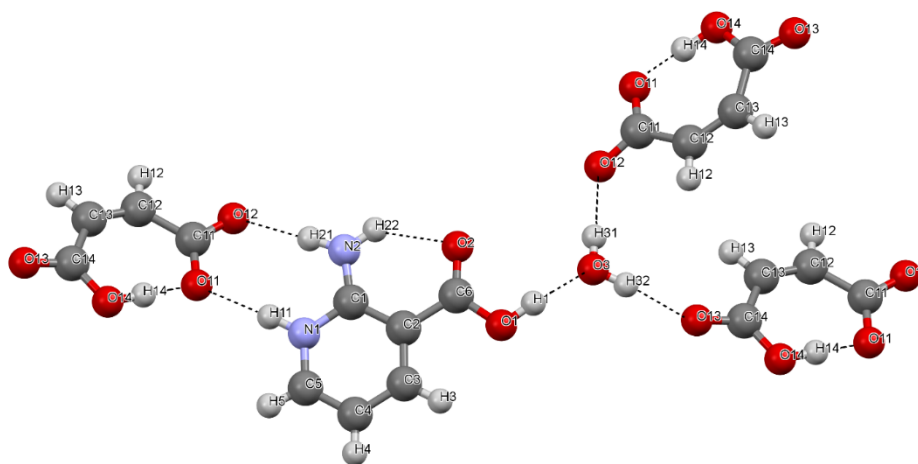


Figure 2. A fragment of the [2AmNic+Mle+H₂O] (1:1:1) crystal structure, illustration of hydrogen bond patterns.

3. Results

3.1. Crystal Structure and H-Bond Network

The relevant crystallographic data for the multicomponent crystals are presented in Supplementary Materials Table S2. The [2AmNic+Fum+H₂O] (1:1:1) crystal has a layered (ribbon) structure. In addition to the R₂²(8) synthon, the dicarboxylic acid anion is stabilized in the layer by two intermolecular O . . . H-O bonds, which form both the oxygen atoms of the COO[−] group, when interacting with the H₂O molecule, and the COOH group of the fumaric acid (Figure 1 and Table 1). According to Reference [40], the latter H-bond can be considered short (Table 1). A water molecule forms three H-bonds: two as a proton donor and one as an acceptor (Figure 1). Two H-bonds formed by the water molecule lie in the layer, while the third interacts with the fumaric acid molecule in an adjacent layer.

The [2AmNic+Mle+H₂O] (1:1:1) crystal does not have a layered (ribbon) structure. This may be due to the presence of an intramolecular H-bond in the maleate anion. As a result, this crystal contains one H-bond less per 1:1:1 trimer than the [2AmNic+Fum+H₂O] crystal (Tables 1 and 2). In both crystals, the water molecule forms three H-bonds (Figure 2), and one of them is short (Table 2). A characteristic feature of the H-bond network in the considered crystals is bifurcate H-bonds formed by the COO[−] group of the dicarboxylic acids. In contrast to Reference [20], all the H-bonds formed by the COO[−] groups are “classical” and rather strong (see Section 3.2). It should be noted that compounds with C=O and P=O groups quite often form bifurcate H-bonds in molecular crystals [41,42], while the formation of such bonds by the COO[−] group is a rather rare phenomenon. Both crystals have a large number of intermolecular H-bonds, with the COO[−] group proton participating in the formation of short (strong) intermolecular H-bonds.

A maleate anion has a very short and practically linear intramolecular O . . . H-O bond (c.f. Tables 1 and 2 in Reference [43]). To identify possible spectral features of this

H-bond, we recorded a terahertz Raman spectrum of the two crystals as well as crystalline fumaric acid (Supplementary Figures S5–S7) and compared it with that of crystalline maleic acid (Figure 4 in Reference [20]). When comparing the spectra of the two crystalline acids, we came to the conclusion that the band at 320 cm^{-1} was due to the vibrations of the intramolecular O...H–O bond. The visualization of this vibration (Supplementary Figure S8) supported this conclusion. The Raman spectrum of the [2AmNic+Mle+H₂O] crystal also exhibits a band in the region of 300 cm^{-1} (Supplementary Figure S2). It follows from Figure 3 that this is caused by vibrations of two intramolecular H-bonds: O...H–O in the maleate anion and O...H–N in the 2-aminonicotinic acid.

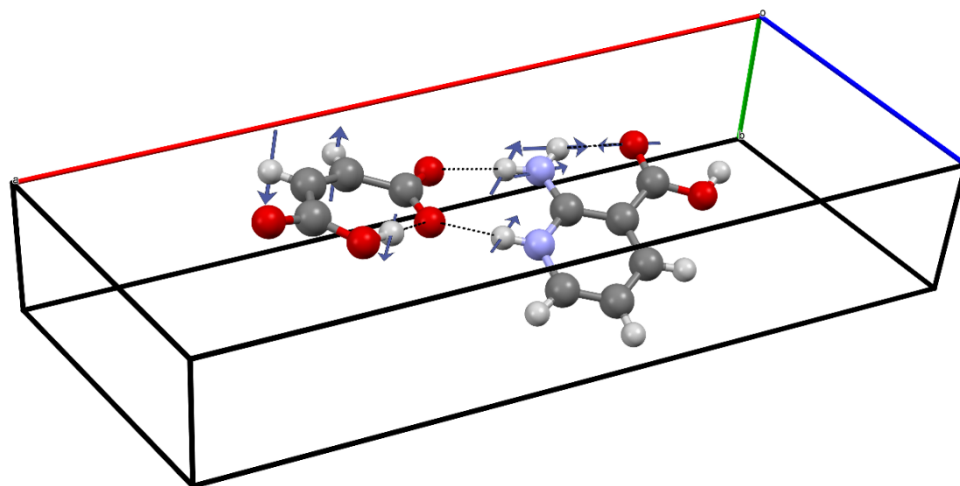


Figure 3. Schematic representation of the Raman active vibration at 316 cm^{-1} of the [2AmNic+Mle+H₂O] crystal, evaluated using periodic DFT computations at the B3LYP/6-31G** level. The arrows indicate the directions of the relative atom displacements.

Unlike crystalline [2AmNic+Fum+H₂O] (1:1:1), two N⁺–H...O[−] bonds in the 8-membered cycle of the [2AmNic+Mle+H₂O] (1:1:1) crystal are almost equivalent (Table 2). This phenomenon can be explained by the presence of an intramolecular H-bond in the maleate ion. To substantiate this assumption, we compared the frequency and shape of the stretching vibrations of the N⁺–H groups in heterodimers of fumaric and maleic anions with a 2-amino-nicotinic acid cation (Supplementary Figure S9). In accordance with the literature data [44], there is strong coupling between the intra- and inter-molecular H-bonds formed by the oxygen of the CO₂[−] group.

3.2. The Structure-Directing Role of the Water Molecule

The molecules or ions that make up multicomponent crystals are held together by various noncovalent interactions, including H-bonds, halogen bonds, and $\pi \cdots \pi$ stacking [40,45–50]. The fine balance between these intermolecular forces is mainly responsible for the physicochemical properties of crystalline materials and plays an important role in determining their packing arrangements and morphology [51]. Although all types of intermolecular interactions contribute to the ultimate stability of the crystal structure, intermolecular H-bonds often play a more prominent role than others due to their strength and directionality [52–55], tailoring the supramolecular architectures of multicomponent crystals and enabling a crystal engineering strategy to be applied [12,56,57]. There are two major groups of multicomponent molecular crystals: cocrystals (that are made from different neutral chemical entities) [6,58] and organic salts (that consist of charged species of components) [8,59]. The lattice energies vary from ~ 160 to ~ 300 kJ/mol, both for cocrystals [60–64] and for organic salts [19,65–68]. It should be noted that the estimation of the lattice energy of organic salts is not straightforward [19].

To elucidate the role of water in the formation of the structure of the considered crystals, we calculated the contribution of the H-bonds formed by a water molecule to the

total energy of the intermolecular H-bonds per a 1:1:1 structural unit. Several schemes for estimating the energy (enthalpy) of intermolecular H-bonds in crystals have been proposed in the literature. In most cases, empirical approaches that are used relate the energy of an intermolecular interaction with a certain electron density parameter at the bond critical point [69–71]. In this case, the calculated values of the electron density, the values of the parameters derived from the precise X-ray diffraction data, and hybrid approaches are used [72]. This gives rise to well-founded criticism [73,74]. To obtain reliable values of the H-bond energies/enthalpies, we used several approaches, two of which estimated the intermolecular H-bond enthalpy from the spectroscopic [75] and metric [76] characteristics of these bonds in the crystals. It should be noted that to estimate the energy of intramolecular H-bonds in the solid state requires the use of other empirical approaches [77,78].

The results are shown in Table 3. In accordance with the literature data [79,80], all the approaches yield values of the energies/enthalpies of weak and moderate H-bonds [40] that are in good agreement with each other. Significant differences in the calculated values are observed only in short (strong) H-bonds ($R(O \cdots O) < 2.6 \text{ \AA}$), which is caused by the contribution of the covalent component to the energy of these bonds [81,82]. All the schemes for estimating energies/enthalpies allow us to conclude that the total energy of hydrogen bonds formed by water molecules is greater than the energy of the $R_2^2(8)$ synthon. According to all of the approaches, the total enthalpies/energies of the H-bonds are about 40% for [2AmNic+Fum+H₂O] and 50% for [2AmNic+Mle+H₂O], respectively. This allows us to conclude that the water molecule determines the structure of the considered multicomponent crystals.

Table 3. Theoretical values of the enthalpy, ΔH_{HB} , and energy, E_{HB} , of intermolecular H-bonds in the crystals evaluated using different empirical approaches. The O \cdots H distances, frequencies of the OH stretching vibrations, and crystalline electron density were calculated at the B3LYP/6-31G** level. The total $\Delta H_{HB}/E_{HB}$ values of the H-bonds formed by the water molecule are indicated in parentheses.

Fragment ¹	R(O \cdots H), Å	$-\Delta H_{HB}$ ² , kJ/mol	$-\Delta H_{HB}$ ³ , kJ/mol	E_{HB} ⁴ , kJ/mol
[2AmNic+Fum+H ₂ O] (1:1:1)				
O12 ... H21-N2	1.840	23.4	-	26.8
O11 ... H11-N1	1.628	34.0	-	45.7
O12 ... H31-O3	1.709	29.3	27.8	35.8
O13 ... H32-O3	2.034	17.2	18.3	24.3
O11 ... H14-O14	1.563	38.5	39.7	52.9
O3 ... H1-O1	1.571	37.9	40.7	52.1
$\Sigma(-\Delta H_{HB}/E_{HB})$	-	180.3 (84.4)	(86.8)	237.6 (112.1)
[2AmNic+Mle+H ₂ O] (1:1:1)				
O12 ... H21-N2	1.792	25.4	-	30.5
O11 ... H11-N1	1.785	25.7	-	30.2
O12 ... H31-O3	1.725	28.5	24.8	34.9
O13 ... H32-O3	1.797	25.2	17.6	28.5
O3 ... H1-O1	1.525	41.5	43.5	58.2
$\Sigma(-\Delta H_{HB}/E_{HB})$	-	146.3 (95.2)	(85.9)	182.3 (121.6)

¹ The atomic numbering is given in Figures 1 and 2. ² Evaluated using the Rozenberg approach [76]: $-\Delta H_{HB} [\text{kJ mol}^{-1}] = 0.134 \cdot R(\text{O} \cdots \text{H})^{-3.05}$, where the $R(\text{H} \cdots \text{O})$ is the H \cdots O distance (nm). ³ Evaluated using the Iogansen approach [75]: $-\Delta H_{HB} [\text{kJ mol}^{-1}] = 1.386 \cdot (\Delta \nu [\text{cm}^{-1}] - 40)^{0.5}$, where $\Delta \nu = \nu(\text{OH}_{\text{free}}) - \nu(\text{OH})$ represents the red-shift value of the OH stretching frequency caused by the formation of the H-bond with the OH group being the proton donor. It should be noted that $\nu(\text{OH}_{\text{free}})$ and $\nu(\text{OH})$ are the frequencies of the localized, uncoupled OH stretching vibration. ⁴ Evaluated using the Espinoza approach [69]: $E_{HB} [\text{kJ mol}^{-1}] = 1124 \cdot G_b$ [atomic units], where G_b is the positively defined local electronic kinetic energy density at the O \cdots H bond critical point.

4. Discussion

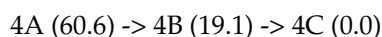
Due to the structural features, many medicinal and bioactive compounds are in the zwitterionic form both in the crystal and in the solution at pH values characteristic of physiological fluids [83,84]. The presence of acidic and basic functional groups in the molecule

structure with close pKa values (the difference is less than 3 units) leads to the formation of amphoteric or zwitterionic compounds. Many zwitterionic medicinal compounds have a high melting point, which is explained by strong intermolecular interactions (primarily H-bonds and dipole–dipole contacts) between the charged fragments of the crystal molecules. Due to the high energy of the crystal lattice and the permanent intramolecular multipole moment, a large number of zwitterionic compounds are poorly soluble in both polar and non-polar solvents [85,86]. In addition, due to the poor membrane permeability, zwitterions have a low absorption rate compared to neutral and even ionized forms, which results in limited bioavailability [84,87,88]. One of the most common methods to solve this problem is salt formation with various organic or inorganic counterions [89]. The formation of a salt with a zwitterionic compound, in most cases, makes the product melting point lower compared to that of the initial zwitterionic form as there are fewer dipole–dipole interactions so that the solubility in polar and non-polar solvents and bioavailability improve [86,90,91]. Despite the large number of publications devoted to the preparation and study of salts of zwitterionic compounds, the process of proton transfer from an acid to a zwitterionic molecule during their formation remains poorly understood.

We chose dicarboxylic acid as it could be used to describe the possible pathway of proton transfer from its COOH group to the COO[−] group of AmNicAc in water. The molecule of maleic acid seems to be the most suitable as its second acidic proton is involved in the formation of the intramolecular H-bond. Fumaric acid is assumed to have a similar proton transfer pathway, but the presence of a second COOH group makes the theoretical model much more complicated. The starting structure was a trimer of maleic acid, 2-amino nicotinic acid, and water (1:1:1), to which we added a minimum number of water molecules that was necessary for proton transfer. It turned out that two additional water molecules were enough to implement the process. These molecules interact with the atoms of the 1:1:1 structure or with each other through H-bonds, the energy of which is much higher than that of the H-bonds in bulk water (the reason for the “strengthening” of the intermolecular H-bonds is the acidic proton of the COOH group and the COO[−] group). The calculations were carried out in the discrete-continuum approximation [92–95] using the Gaussian16 program [96]. The bulk water was described by the polarizable continuum model [96]. The calculations were carried out in the B3LYP/6-311++G** approximation.

The initial structure is shown in Figure 4A. In accordance with the literature data [26], the acidic proton goes to the neighboring water molecule and then, by the “relay mechanism”, moves to the COO[−] group of the amino acid. As a result of the synchronous transfer of the “acidic” proton along the H-bonds chain (along the water wire) and the intramolecular transition of the proton in the N...H...O fragment, the structure in Figure 4B is formed. Then, the maleate ion rotates by ~90 degrees and the “first” solvation shell is rearranged, i.e., the structure in Figure 4C is formed, which is very close to the structure realized in the crystal, see Figure 2.

The process scheme is shown below. The relative stability of the structures is given in parentheses (the sum of the electronic and zero-point energies) in kJ/mol:



This process can be modeled by ab initio molecular dynamics simulations using relatively small cells [97]. However, such modeling is beyond the scope of this work.

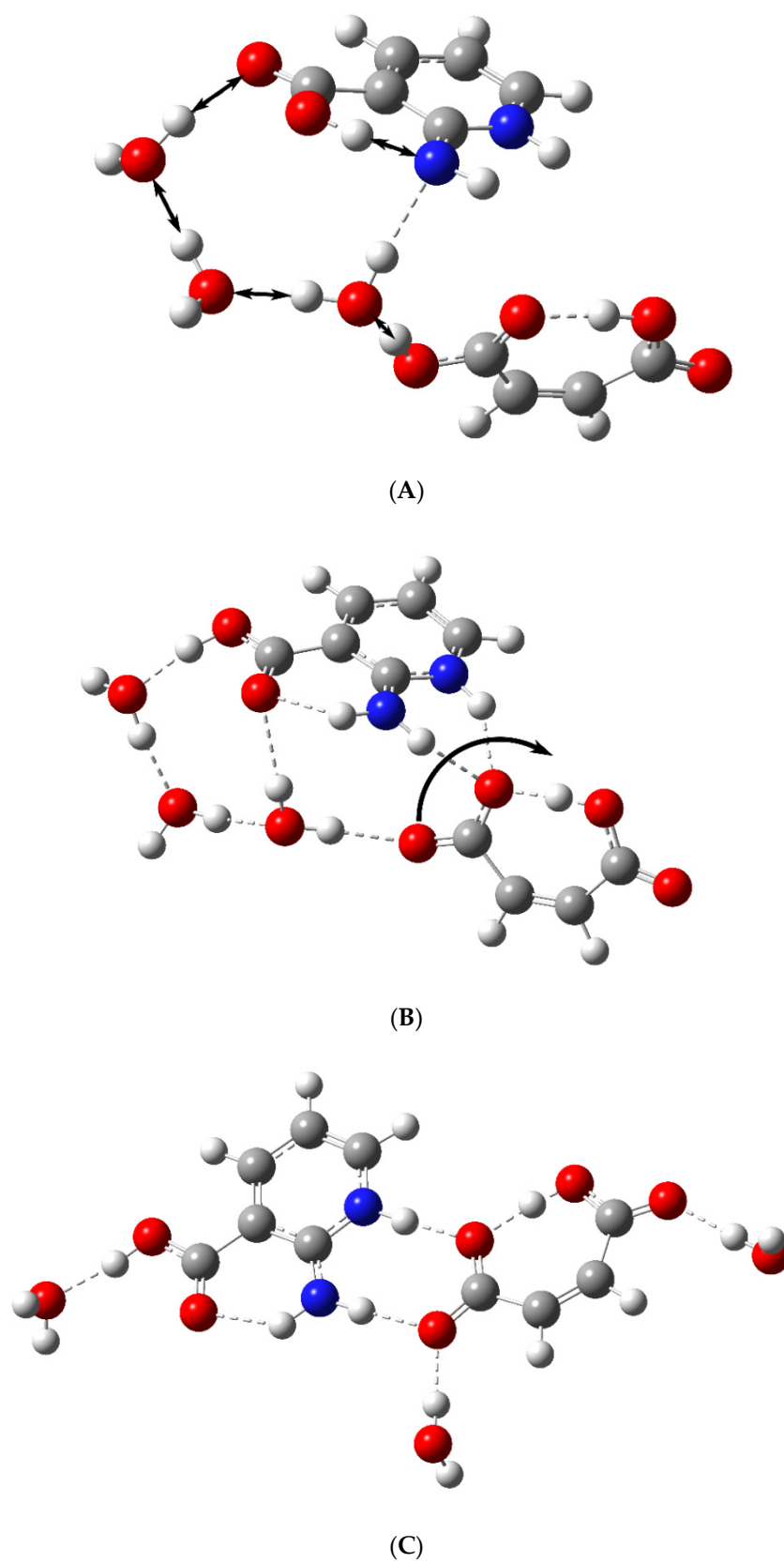


Figure 4. Structures used in the process of proton transfer modeling. The initial structure (A); the intermediate structure (B); the final structure (C).

5. Conclusions

The structure and H-bond network in two multicomponent crystals—[2AmNic+Fum+H₂O] (1:1:1) and [2AmNic+Mle+H₂O] (1:1:1)—are characterized by X-ray analysis, terahertz Raman spectroscopy, and periodic DFT calculations. The intramolecular H-bonds cause the appearance of a Raman-active band around 300 cm⁻¹ in the [2AmNic+Mle+H₂O] (1:1:1) crystal. The total enthalpy of the intermolecular H-bonds in these crystals, estimated per a 1:1:1 structural unit, is about 160 kJ/mol; moreover, the water molecule accounts for about 90 kJ/mol. This allows us to conclude that the water molecule determines the structure of the considered multicomponent crystals. A scheme of the transfer of a dicarboxylic acid proton to a zwitterionic amino acid molecule in the process of the [2AmNic+Fum+H₂O] (1:1:1) and [2AmNic+Mle+H₂O] (1:1:1) formation in the polar protic solvent is proposed. Water molecules were found to play the key role in this process, forming a “water wire” between the COOH group of the dicarboxylic acid and the COO⁻ group of the zwitterion.

Supplementary Materials: The following are available online at <https://www.mdpi.com/2073-8994/13/3/425/s1>, Section S1: Computational details; Table S1: Theoretical values of the enthalpy, ΔH_{HB} , and energy, E_{HB} , of intermolecular H-bonds in the [2AmNic+Fum+H₂O] (1:1:1) crystal evaluated using several empirical approaches; Figures S1 and S2: calculated and experimental PXRD patterns; Figures S3 and S4: DSC and TG traces; Figure S5: Raman spectrum of the [2AmNic+Fum+H₂O] (1:1:1) crystal. Experiment (black line) vs. B3LYP/6-31G** computations (red bars); Figure S6: Raman spectrum of the [2AmNic+Mle+H₂O] (1:1:1) crystal. Experiment (black line) vs. B3LYP/6-31G** computations (red bars); Figure S7: Raman spectrum of crystalline fumaric acid. Experiment (black line) vs. B3LYP/6-31G** computations (red bars); Figure S8: Schematic representation of the Raman active vibration at 337 cm⁻¹ of crystalline maleic acid, evaluated using periodic DFT computations at the B3LYP/6-31G** level; Figure S9: Schematic representation of the IR active vibration at 2524 cm⁻¹ of the fumaric acid-2-amino-nicotinic acid zwitterion heterodimer (the upper panel) and 2636 cm⁻¹ of the maleic acid-2-amino-nicotinic acid zwitterion (the lower panel), evaluated using DFT computations at the B3LYP/6-31G** level; Table S2: Crystallographic data for [2AmNic+Fum+H₂O] (1:1:1) and [2AmNic+Mle+H₂O] (1:1:1) multicomponent crystals.

Author Contributions: Conceptualization, A.O.S. and M.V.V.; experimental methodology, A.O.S. and N.A.V.; theoretical methodology, M.V.V.; investigation, A.O.S., N.A.V., A.V.C., O.D.P., S.V.A., O.A.A., D.E.M. and M.V.V.; single-crystal XRD experiment, A.V.C.; Raman spectroscopy, O.D.P.; writing and visualization, A.O.S. and M.V.V.; supervision, M.V.V. and A.O.S.; project administration, A.O.S.; funding acquisition, A.O.S. All authors have read and agreed to the published version of the manuscript.

Funding: The work was supported by the Russian Science Foundation (project No. 19-73-10005).

Institutional Review Board Statement: Not applicable.

Informed Consent Statement: Not applicable.

Data Availability Statement: The Raman spectra and I/O files are available from the respective author upon reasonable request.

Acknowledgments: The experimental Raman spectra were obtained at Lomonosov Moscow State University using the equipment purchased under the Lomonosov Moscow State University Program of Development. M.V.V. thanks Alexander P. Voronin (G.A. Krestov Institute of Solution Chemistry of RAS) for performing the Bader analysis of the crystal electron density.

Conflicts of Interest: The authors declare no conflict of interest.

References

1. Schwoerer, M.; Wolf, H.C. *Organic Molecular Solids*; Wiley: Weinheim, Germany, 2008.
2. Qiu, Y.; Chen, Y.; Zhang, G.G.Z.; Yu, L.; Mantri, R.V. *Developing Solid Oral Dosage Forms: Pharmaceutical Theory and Practice*; Elsevier Science: London, UK, 2016.
3. Sathisaran, I.; Dalvi, S.V. Engineering Cocrystals of Poorly Water-Soluble Drugs to Enhance Dissolution in Aqueous Medium. *Pharmaceutics* **2018**, *10*, 108. [[CrossRef](#)] [[PubMed](#)]

4. Sun, L.; Wang, Y.; Yang, F.; Zhang, X.; Hu, W. Cocrystal Engineering: A Collaborative Strategy toward Functional Materials. *Adv. Mater.* **2019**, *31*, 1902328. [[CrossRef](#)]
5. Kavanagh, O.N.; Croker, D.M.; Walker, G.M.; Zaworotko, M.J. Pharmaceutical cocrystals: From serendipity to design to application. *Drug Discov. Today* **2019**, *24*, 796–804. [[CrossRef](#)]
6. Duggirala, N.K.; Perry, M.L.; Almarsson, Ö.; Zaworotko, M.J. Pharmaceutical cocrystals: Along the path to improved medicines. *Chem. Commun.* **2016**, *52*, 640–655. [[CrossRef](#)] [[PubMed](#)]
7. Bolla, G.; Nangia, A. Pharmaceutical cocrystals: Walking the talk. *Chem. Commun.* **2016**, *52*, 8342–8360. [[CrossRef](#)] [[PubMed](#)]
8. Berry, D.J.; Steed, J.W. Pharmaceutical cocrystals, salts and multicomponent systems; intermolecular interactions and property based design. *Adv. Drug Del. Rev.* **2017**, *117*, 3–24. [[CrossRef](#)] [[PubMed](#)]
9. Aakeröy, C.B.; Hussain, I.; Desper, J. 2-Acetaminopyridine: A Highly Effective Cocrystallizing Agent. *Cryst. Growth Des.* **2006**, *6*, 474–480. [[CrossRef](#)]
10. Aakeröy, C.B.; Forbes, S.; Desper, J. Altering physical properties of pharmaceutical co-crystals in a systematic manner. *CrystEngComm* **2014**, *16*, 5870–5877. [[CrossRef](#)]
11. Walsh, R.D.B.; Bradner, M.W.; Fleischman, S.; Morales, L.A.; Moulton, B.; Rodríguez-Hornedo, N.; Zaworotko, M.J. Crystal engineering of the composition of pharmaceutical phases. *Chem. Commun.* **2003**, *2*, 186–187. [[CrossRef](#)] [[PubMed](#)]
12. Corpinot, M.K.; Bučar, D.-K. A Practical Guide to the Design of Molecular Crystals. *Cryst. Growth Des.* **2019**, *19*, 1426–1453. [[CrossRef](#)]
13. Desiraju, G.R. Supramolecular Synthons in Crystal Engineering—A New Organic Synthesis. *Angew. Chem. Int. Ed. Engl.* **1995**, *34*, 2311–2327. [[CrossRef](#)]
14. Lemmerer, A.; Bernstein, J.; Kahlenberg, V. One-pot covalent and supramolecular synthesis of pharmaceutical co-crystals using the API isoniazid: A potential supramolecular reagent. *CrystEngComm* **2010**, *12*, 2856–2864. [[CrossRef](#)]
15. Desiraju, G.R. Crystal Engineering: From Molecule to Crystal. *J. Am. Chem. Soc.* **2013**, *135*, 9952–9967. [[CrossRef](#)] [[PubMed](#)]
16. Desiraju, G.R. Crystal Engineering: A Holistic View. *Angew. Chem. Int. Ed.* **2007**, *46*, 8342–8356. [[CrossRef](#)] [[PubMed](#)]
17. Surov, A.O.; Voronin, A.P.; Vener, M.V.; Churakov, A.V.; Perlovich, G.L. Specific features of supramolecular organisation and hydrogen bonding in proline cocrystals: A case study of fenamates and diclofenac. *CrystEngComm* **2018**, *20*, 6970–6981. [[CrossRef](#)]
18. Bolla, G.; Nangia, A. Novel pharmaceutical salts of albendazole. *CrystEngComm* **2018**, *20*, 6394–6405. [[CrossRef](#)]
19. Voronin, A.P.; Surov, A.O.; Churakov, A.V.; Parashchuk, O.D.; Rykounov, A.A.; Vener, M.V. Combined X-ray Crystallographic, IR/Raman Spectroscopic, and Periodic DFT Investigations of New Multicomponent Crystalline Forms of Anthelmintic Drugs: A Case Study of Carbendazim Maleate. *Molecules* **2020**, *25*, 2386. [[CrossRef](#)] [[PubMed](#)]
20. Mirzaei, M.; Sadeghi, F.; Molčanov, K.; Zaręba, J.K.; Gomila, R.M.; Frontera, A. Recurrent Supramolecular Motifs in a Series of Acid–Base Adducts Based on Pyridine-2,5-Dicarboxylic Acid N-Oxide and Organic Bases: Inter- and Intramolecular Hydrogen Bonding. *Cryst. Growth Des.* **2020**, *20*, 1738–1751. [[CrossRef](#)]
21. Yadav, B.; Balasubramanian, S.; Chavan, R.B.; Thipparaboina, R.; Naidu, V.G.M.; Shastri, N.R. Hepatoprotective Cocrystals and Salts of Riluzole: Prediction, Synthesis, Solid State Characterization, and Evaluation. *Cryst. Growth Des.* **2018**, *18*, 1047–1061. [[CrossRef](#)]
22. Thomas, S.P.; Kumar, V.; Alhameedi, K.; Guru Row, T.N. Non-Classical Synthons: Supramolecular Recognition by S... O Chalcogen Bonding in Molecular Complexes of Riluzole. *Chem. Eur. J.* **2019**, *25*, 3591–3597. [[CrossRef](#)] [[PubMed](#)]
23. Babu, N.J.; Reddy, L.S.; Nangia, A. Amide–N-Oxide Heterosynthon and Amide Dimer Homosynthon in Cocrystals of Carboxamide Drugs and Pyridine N-Oxides. *Mol. Pharm.* **2007**, *4*, 417–434. [[CrossRef](#)] [[PubMed](#)]
24. Dunitz, J.D.; Gavezzotti, A. Supramolecular Synthons: Validation and Ranking of Intermolecular Interaction Energies. *Cryst. Growth Des.* **2012**, *12*, 5873–5877. [[CrossRef](#)]
25. Vener, M.V.; Levina, E.O.; Koloskov, O.A.; Rykounov, A.A.; Voronin, A.P.; Tsirelson, V.G. Evaluation of the lattice energy of the two-component molecular crystals using solid-state density functional theory. *Cryst. Growth Des.* **2014**, *14*, 4997–5003. [[CrossRef](#)]
26. Xu, J.; Zhang, Y.; Voth, G.A. Infrared Spectrum of the Hydrated Proton in Water. *J. Phys. Chem. Lett.* **2011**, *2*, 81–86. [[CrossRef](#)] [[PubMed](#)]
27. Kaila, V.R.I.; Hummer, G. Energetics and dynamics of proton transfer reactions along short water wires. *PCCP* **2011**, *13*, 13207–13215. [[CrossRef](#)] [[PubMed](#)]
28. Zatula, A.S.; Ryding, M.J.; Uggerud, E. Concerted proton migration along short hydrogen bonded water bridges in bipyridine–water clusters. *PCCP* **2012**, *14*, 13907–13909. [[CrossRef](#)] [[PubMed](#)]
29. Freier, E.; Wolf, S.; Gerwert, K. Proton transfer via a transient linear water-molecule chain in a membrane protein. *Proc. Natl. Acad. Sci. USA* **2011**, *108*, 11435–11439. [[CrossRef](#)]
30. Di Donato, M.; van Wilderen, L.J.G.W.; Van Stokkum, I.H.M.; Stuart, T.C.; Kennis, J.T.M.; Hellingwerf, K.J.; van Grondelle, R.; Groot, M.L. Proton transfer events in GFP. *PCCP* **2011**, *13*, 16295–16305. [[CrossRef](#)] [[PubMed](#)]
31. Grigorenko, B.; Polyakov, I.; Nemukhin, A. Mechanisms of ATP to cAMP Conversion Catalyzed by the Mammalian Adenylyl Cyclase: A Role of Magnesium Coordination Shells and Proton Wires. *J. Phys. Chem. B* **2020**, *124*, 451–460. [[CrossRef](#)] [[PubMed](#)]
32. Sheldrick, G. *SADABS, Program for Scaling and Correction of Area Detector Data*; University of Göttingen: Lower Saxony, Germany, 1997.
33. Sheldrick, G. A short history of SHELX. *Acta Cryst. Sect. A Found. Cryst.* **2008**, *64*, 112–122. [[CrossRef](#)] [[PubMed](#)]

34. Dovesi, R.; Erba, A.; Orlando, R.; Zicovich-Wilson, C.M.; Civalieri, B.; Maschio, L.; Rérat, M.; Casassa, S.; Baima, J.; Salustro, S.; et al. Quantum-mechanical condensed matter simulations with CRYSTAL. *WIREs Comput. Mol. Sci.* **2018**, *8*, e1360. [[CrossRef](#)]
35. Becke, A.D. Density-functional thermochemistry. III. The role of exact exchange. *J. Chem. Phys.* **1993**, *98*, 5648–5652. [[CrossRef](#)]
36. Vosko, S.H.; Wilk, L.; Nusair, M. Accurate spin-dependent electron liquid correlation energies for local spin density calculations: A critical analysis. *Can. J. Phys.* **1980**, *58*, 1200–1211. [[CrossRef](#)]
37. Perdew, J.P.; Burke, K.; Ernzerhof, M. Generalized Gradient Approximation Made Simple. *Phys. Rev. Lett.* **1996**, *77*, 3865–3868. [[CrossRef](#)] [[PubMed](#)]
38. Grimme, S.; Antony, J.; Ehrlich, S.; Krieg, H. A consistent and accurate ab initio parametrization of density functional dispersion correction (DFT-D) for the 94 elements H-Pu. *J. Chem. Phys.* **2010**, *132*, 154104. [[CrossRef](#)]
39. Grimme, S.; Ehrlich, S.; Goerigk, L. Effect of the damping function in dispersion corrected density functional theory. *J. Comput. Chem.* **2011**, *32*, 1456–1465. [[CrossRef](#)]
40. Steiner, T. The Hydrogen Bond in the Solid State. *Angew. Chem. Int. Ed.* **2002**, *41*, 48–76. [[CrossRef](#)]
41. Rozas, I.; Alkorta, I.; Elguero, J. Bifurcated Hydrogen Bonds: Three-Centered Interactions. *J. Phys. Chem. A* **1998**, *102*, 9925–9932. [[CrossRef](#)]
42. Tupikina, E.Y.; Bodensteiner, M.; Tolstoy, P.M.; Denisov, G.S.; Shenderovich, I.G. P=O Moiety as an Ambidextrous Hydrogen Bond Acceptor. *J. Phys. Chem. C* **2018**, *122*, 1711–1720. [[CrossRef](#)]
43. Vener, M.V. Model study of the primary H/D isotope effects on the NMR chemical shift in strong hydrogen-bonded systems. *Chem. Phys.* **1992**, *166*, 311–316. [[CrossRef](#)]
44. Józwiak, K.; Jezierska, A.; Panek, J.J.; Goremychkin, E.A.; Tolstoy, P.M.; Shenderovich, I.G.; Filarowski, A. Inter- vs. Intramolecular Hydrogen Bond Patterns and Proton Dynamics in Nitrophthalic Acid Associates. *Molecules* **2020**, *25*, 4720. [[CrossRef](#)]
45. Müller-Dethlefs, K.; Hobza, P. Noncovalent Interactions: A Challenge for Experiment and Theory. *Chem. Rev.* **2000**, *100*, 143–168. [[CrossRef](#)] [[PubMed](#)]
46. Aakeröy, C.B.; Evans, T.A.; Seddon, K.R.; Pálinkó, I. The C–H . . . Cl hydrogen bond: Does it exist? *New J. Chem.* **1999**, *23*, 145–152. [[CrossRef](#)]
47. Nishio, M. CH/ π hydrogen bonds in crystals. *CrystEngComm* **2004**, *6*, 130–158. [[CrossRef](#)]
48. Martinez, C.R.; Iverson, B.L. Rethinking the term “ π -stacking”. *Chem. Sci.* **2012**, *3*, 2191–2201. [[CrossRef](#)]
49. Bartashevich, E.V.; Tsirelson, V.G. Interplay between non-covalent interactions in complexes and crystals with halogen bonds. *Russ. Chem. Rev.* **2014**, *83*, 1181–1203. [[CrossRef](#)]
50. Melikova, S.M.; Voronin, A.P.; Panek, J.; Frolov, N.E.; Shishkina, A.V.; Rykounov, A.A.; Tretyakov, P.Y.; Vener, M.V. Interplay of π -stacking and inter-stacking interactions in two-component crystals of neutral closed-shell aromatic compounds: Periodic DFT study. *RSC Adv.* **2020**, *10*, 27899–27910. [[CrossRef](#)]
51. Mattei, A.; Li, T. Intermolecular Interactions and Computational Modeling. In *Pharmaceutical Crystals*; John Wiley & Sons: Hoboken, USA, 2018; pp. 123–167. [[CrossRef](#)]
52. Burrows, A.D. Crystal Engineering Using Multiple Hydrogen Bonds. In *Supramolecular Assembly via Hydrogen Bonds I*; Mingos, D.M.P., Ed.; Springer: Berlin/Heidelberg, Germany, 2004; pp. 55–96. [[CrossRef](#)]
53. Aakeröy, C.B.; Seddon, K.R. The hydrogen bond and crystal engineering. *Chem. Soc. Rev.* **1993**, *22*, 397–407. [[CrossRef](#)]
54. Subramanian, S.; Zaworotko, M.J. Exploitation of the hydrogen bond: Recent developments in the context of crystal engineering. *Coord. Chem. Rev.* **1994**, *137*, 357–401. [[CrossRef](#)]
55. Desiraju, G.R. Designer crystals: Intermolecular interactions, network structures and supramolecular synthons. *Chem. Commun.* **1997**, *16*, 1475–1482. [[CrossRef](#)]
56. Bhattacharya, S.; Peraka, K.S.; Zaworotko, M.J. Chapter 2 The Role of Hydrogen Bonding in Co-crystals. In *Co-Crystals: Preparation, Characterization and Applications*; The Royal Society of Chemistry: Croydon, UK, 2018; pp. 33–79. [[CrossRef](#)]
57. Medvedev, A.G.; Churakov, A.V.; Prikhodchenko, P.V.; Lev, O.; Vener, M.V. Crystalline Peroxosolvates: Nature of the Cofomer, Hydrogen-Bonded Networks and Clusters, Intermolecular Interactions. *Molecules* **2021**, *26*, 26. [[CrossRef](#)] [[PubMed](#)]
58. Aakeröy, C.B.; Salmon, D.J. Building co-crystals with molecular sense and supramolecular sensibility. *CrystEngComm* **2005**, *7*, 439–448. [[CrossRef](#)]
59. Elder, D.P.; Holm, R.; Diego, H.L.d. Use of pharmaceutical salts and cocrystals to address the issue of poor solubility. *Int. J. Pharm.* **2013**, *453*, 88–100. [[CrossRef](#)] [[PubMed](#)]
60. Manin, A.N.; Voronin, A.P.; Shishkina, A.V.; Vener, M.V.; Churakov, A.V.; Perlovich, G.L. Influence of Secondary Interactions on the Structure, Sublimation Thermodynamics, and Solubility of Salicylate:4-Hydroxybenzamide Cocrystals. Combined Experimental and Theoretical Study. *J. Phys. Chem. B* **2015**, *119*, 10466–10477. [[CrossRef](#)] [[PubMed](#)]
61. Voronin, A.P.; Perlovich, G.L.; Vener, M.V. Effects of the crystal structure and thermodynamic stability on solubility of bioactive compounds: DFT study of isoniazid cocrystals. *Comput. Theor. Chem.* **2016**, *1092*, 1–11. [[CrossRef](#)]
62. Landeros-Rivera, B.; Moreno-Esparza, R.; Hernández-Trujillo, J. Theoretical study of intermolecular interactions in crystalline arene-perhaloarene adducts in terms of the electron density. *RSC Adv.* **2016**, *6*, 77301–77309. [[CrossRef](#)]
63. Jarzemska, K.N.; Hoser, A.A.; Varughese, S.; Kamiński, R.; Malinska, M.; Stachowicz, M.; Pedireddi, V.R.; Woźniak, K. Structural and Energetic Analysis of Molecular Assemblies in a Series of Nicotinamide and Pyrazinamide Cocrystals with Dihydroxybenzoic Acids. *Cryst. Growth Des.* **2017**, *17*, 4918–4931. [[CrossRef](#)]

64. Tao, Q.; Hao, Q.-Q.; Voronin, A.P.; Dai, X.-L.; Huang, Y.; Perlovich, G.L.; Lu, T.-B.; Chen, J.-M. Polymorphic Forms of a Molecular Salt of Phenazopyridine with 3,5-Dihydroxybenzoic Acid: Crystal Structures, Theoretical Calculations, Thermodynamic Stability, and Solubility Aspects. *Cryst. Growth Des.* **2019**, *19*, 5636–5647. [[CrossRef](#)]
65. Manin, A.N.; Voronin, A.P.; Drozd, K.V.; Churakov, A.V.; Perlovich, G.L. Pharmaceutical salts of emoxypine with dicarboxylic acids. *Acta Crystallogr. Sect. C* **2018**, *74*, 797–806. [[CrossRef](#)] [[PubMed](#)]
66. Surov, A.O.; Churakov, A.V.; Perlovich, G.L. Three Polymorphic Forms of Ciprofloxacin Maleate: Formation Pathways, Crystal Structures, Calculations, and Thermodynamic Stability Aspects. *Cryst. Growth Des.* **2016**, *16*, 6556–6567. [[CrossRef](#)]
67. Surov, A.O.; Voronin, A.P.; Simagina, A.A.; Churakov, A.V.; Skachilova, S.Y.; Perlovich, G.L. Saccharin salts of biologically active hydrazone derivatives. *New J. Chem.* **2015**, *39*, 8614–8622. [[CrossRef](#)]
68. Chan, H.C.S.; Kendrick, J.; Neumann, M.A.; Leusen, F.J.J. Towards ab initio screening of co-crystal formation through lattice energy calculations and crystal structure prediction of nicotinamide, isonicotinamide, picolinamide and paracetamol multi-component crystals. *CrystEngComm* **2013**, *15*, 3799–3807. [[CrossRef](#)]
69. Mata, I.; Alkorta, I.; Espinosa, E.; Molins, E. Relationships between interaction energy, intermolecular distance and electron density properties in hydrogen bonded complexes under external electric fields. *Chem. Phys. Lett.* **2011**, *507*, 185–189. [[CrossRef](#)]
70. Kuznetsov, M.L. Can halogen bond energy be reliably estimated from electron density properties at bond critical point? The case of the (A)nZ—Y . . . X— (X, Y = F, Cl, Br) interactions. *Int. J. Quantum Chem.* **2019**, *119*, e25869. [[CrossRef](#)]
71. Emamian, S.; Lu, T.; Kruse, H.; Emamian, H. Exploring Nature and Predicting Strength of Hydrogen Bonds: A Correlation Analysis Between Atoms-in-Molecules Descriptors, Binding Energies, and Energy Components of Symmetry-Adapted Perturbation Theory. *J. Comput. Chem.* **2019**, *40*, 2868–2881. [[CrossRef](#)] [[PubMed](#)]
72. Korlyukov, A.A.; Nelyubina, Y.V. Quantum chemical methods in charge density studies from X-ray diffraction data. *Russ. Chem. Rev.* **2019**, *88*, 677–716. [[CrossRef](#)]
73. Dem'yanov, P.; Polestshuk, P. A Bond Path and an Attractive Ehrenfest Force Do Not Necessarily Indicate Bonding Interactions: Case Study on M2X2 (M = Li, Na, K; X = H, OH, F, Cl). *Chem. Eur. J.* **2012**, *18*, 4982–4993. [[CrossRef](#)] [[PubMed](#)]
74. Shahbazian, S. Why Bond Critical Points Are Not “Bond” Critical Points. *Chem. Eur. J.* **2018**, *24*, 5401–5405. [[CrossRef](#)] [[PubMed](#)]
75. Iogansen, A.V. Direct proportionality of the hydrogen bonding energy and the intensification of the stretching $\nu(\text{XH})$ vibration in infrared spectra. *Spectrochim. Acta Part A Mol. Biomol. Spectrosc.* **1999**, *55*, 1585–1612. [[CrossRef](#)]
76. Rozenberg, M.; Loewenschuss, A.; Marcus, Y. An empirical correlation between stretching vibration redshift and hydrogen bond length. *PCCP* **2000**, *2*, 2699–2702. [[CrossRef](#)]
77. Musin, R.N.; Mariam, Y.H. An integrated approach to the study of intramolecular hydrogen bonds in malonaldehyde enol derivatives and naphthazarin: Trend in energetic versus geometrical consequences. *J. Phys. Org. Chem.* **2006**, *19*, 425–444. [[CrossRef](#)]
78. Filarowski, A.; Koll, A.; Sobczyk, L. Intramolecular Hydrogen Bonding in o-hydroxy Aryl Schiff Bases. *Curr. Org. Chem.* **2009**, *13*, 172–193. [[CrossRef](#)]
79. Medvedev, A.G.; Mikhaylov, A.A.; Chernyshov, I.Y.; Vener, M.V.; Lev, O.; Prikhodchenko, P.V. Effect of aluminum vacancies on the H₂O₂ or H₂O interaction with a gamma-AlOOH surface. A solid-state DFT study. *Int. J. Quantum Chem.* **2019**, *119*, e25920. [[CrossRef](#)]
80. Musso, F.; Casassa, S.; Corno, M.; Ugliengo, P. How strong are H-bonds at the fully hydroxylated silica surfaces? Insights from the B3LYP electron density topological analysis. *Struct. Chem.* **2017**, *28*, 1009–1015. [[CrossRef](#)]
81. Vener, M.V.; Manaev, A.V.; Egorova, A.N.; Tsirelson, V.G. QTAIM Study of Strong H-Bonds with the O—H . . . A Fragment (A=O, N) in Three-Dimensional Periodical Crystals. *J. Phys. Chem. A* **2007**, *111*, 1155–1162. [[CrossRef](#)]
82. Grabowski, S.J. What Is the Covalency of Hydrogen Bonding? *Chem. Rev.* **2011**, *111*, 2597–2625. [[CrossRef](#)]
83. Mazák, K.; Noszál, B. Physicochemical Properties of Zwitterionic Drugs in Therapy. *ChemMedChem* **2020**, *15*, 1102–1110. [[CrossRef](#)]
84. Yang, Z.; Li, Q.; Yang, G. Zwitterionic structures: From physicochemical properties toward computer-aided drug designs. *Future Med. Chem.* **2016**, *8*, 2245–2262. [[CrossRef](#)] [[PubMed](#)]
85. Mesallati, H.; Mugheirbi, N.A.; Tajber, L. Two Faces of Ciprofloxacin: Investigation of Proton Transfer in Solid State Transformations. *Cryst. Growth Des.* **2016**, *16*, 6574–6585. [[CrossRef](#)]
86. Mazzenga, G.C.; Berner, B. The transdermal delivery of zwitterionic drugs I: The solubility of zwitterion salts. *J. Control. Release* **1991**, *16*, 77–88. [[CrossRef](#)]
87. Gunnam, A.; Suresh, K.; Ganduri, R.; Nangia, A. Crystal engineering of a zwitterionic drug to neutral cocrystals: A general solution for floxacins. *Chem. Commun.* **2016**, *52*, 12610–12613. [[CrossRef](#)] [[PubMed](#)]
88. Manallack, D.T.; Prankerd, R.J.; Yuriev, E.; Oprea, T.I.; Chalmers, D.K. The significance of acid/base properties in drug discovery. *Chem. Soc. Rev.* **2013**, *42*, 485–496. [[CrossRef](#)] [[PubMed](#)]
89. Stahl, P.H.; Wermuth, C.G.; Pure, I.U.o.; Chemistry, A. *Handbook of Pharmaceutical Salts Properties, Selection, and Use*; Wiley: Weinheim, Germany, 2008.
90. Han, H.-K.; Choi, H.-K. Improved absorption of meloxicam via salt formation with ethanolamines. *Eur. J. Pharm. Biopharm.* **2007**, *65*, 99–103. [[CrossRef](#)] [[PubMed](#)]
91. Gwak, H.-S.; Choi, J.-S.; Choi, H.-K. Enhanced bioavailability of piroxicam via salt formation with ethanolamines. *Int. J. Pharm.* **2005**, *297*, 156–161. [[CrossRef](#)] [[PubMed](#)]

92. Tunon, I.; Rinaldi, D.; Ruiz-Lopez, M.F.; Rivail, J.L. Hydroxide Ion in Liquid Water: Structure, Energetics, and Proton Transfer Using a Mixed Discrete-Continuum ab Initio Model. *J. Phys. Chem.* **1995**, *99*, 3798–3805. [[CrossRef](#)]
93. Nemukhin, A.V.; Topol, I.A.; Grigorenko, B.L.; Burt, S.K. On the Origin of Potential Barrier for the Reaction $\text{OH}^- + \text{CO}_2 \rightarrow \text{HCO}_3^-$ in Water: Studies by Using Continuum and Cluster Solvation Methods. *J. Phys. Chem. B* **2002**, *106*, 1734–1740. [[CrossRef](#)]
94. da Silva, E.F.; Svendsen, H.F.; Merz, K.M. Explicitly Representing the Solvation Shell in Continuum Solvent Calculations. *J. Phys. Chem. A* **2009**, *113*, 6404–6409. [[CrossRef](#)] [[PubMed](#)]
95. Vener, M.V.; Shenderovich, I.G.; Rykounov, A.A. A qualitative study of the effect of a counterion and polar environment on the structure and spectroscopic signatures of a hydrated hydroxyl anion. *Theor. Chem. Acc.* **2013**, *132*, 1361. [[CrossRef](#)]
96. Frisch, M.J.; Trucks, G.W.; Schlegel, H.B.; Scuseria, G.E.; Robb, M.A.; Cheeseman, J.R.; Scalmani, G.; Barone, V.; Petersson, G.A.; Nakatsuji, H.; et al. *Gaussian 16 Rev. C.01*; Gaussian, Inc.: Wallingford, CT, USA, 2016.
97. Sun, J.; Bousquet, D.; Forbert, H.; Marx, D. Glycine in aqueous solution: Solvation shells, interfacial water, and vibrational spectroscopy from ab initio molecular dynamics. *J. Chem. Phys.* **2010**, *133*, 114508. [[CrossRef](#)]